

PFC/JA-96-11

**Multi-Megawatt Relativistic Harmonic
Gyrotron Traveling -Wave Tube
Amplifier Experiments**

W. L. Menninger, B. G. Danly, R. J. Temkin

March, 1996

Dr. William Menninger was with the MIT Plasma Fusion Center. He is currently with Hughes Electron Dynamics Division, P. O. Box 2999, Torrance, CA 90509-9899.

Dr. Bruce Danly was with the MIT Plasma Fusion Center. He is currently at the Naval Research Laboratory, Code 6843, Washington, DC 20375-5347.

This paper has been accepted for publication in the IEEE Trans. Plasma Science. Expected publication date is June, 1996.

This work was supported by the US Dept. of Energy, Division of High Energy Physics under contract DE-FG02-91ER40648 and the US Dept. of Energy, Advanced Energy Projects Office, under contract DE-FG02-89ER-14052.

Multi-megawatt Relativistic Harmonic Gyrotron Traveling-Wave Tube Amplifier Experiments

W.L. Menninger, B.G. Danly, R.J. Temkin

Massachusetts Institute of Technology

Plasma Fusion Center, Cambridge, 02139

This work supported by the U.S. Department of Energy, Advanced Energy Projects Office, under contract DE-FG02-89ER-14052 and by the U.S. Department of Energy Division of High Energy Physics under contract DE-FG02-91ER40648.

1 Abstract

The first multi-megawatt (4 MW, $\eta = 8\%$) harmonic ($\omega = s\Omega_c, s = 2, 3$) relativistic gyrotron traveling-wave tube (gyro-twt) amplifier experiment has been designed, built, and tested. Results from this experimental setup, including the first ever reported third harmonic gyro-twt results, are presented. Operation frequency is 17.1 GHz. Detailed phase measurements are also presented. The electron beam source is SNOMAD-II, a solid-state nonlinear magnetic accelerator driver with nominal parameters of 400 kV and 350 A. The flat-top pulse width is 30 ns. The electron beam is focused using a Pierce geometry and then imparted with transverse momentum using a bifilar helical wiggler magnet. The imparted beam pitch is $\alpha \equiv \beta_{\perp}/\beta_{\parallel} \approx 1$.

Experimental operation involving both a second harmonic interaction with the TE_{21} mode and a third harmonic interaction with the TE_{31} mode, both at 17 GHz, has been characterized. The third harmonic interaction resulted in 4 MW output power and 50 dB single-pass gain, with an efficiency of up to $\sim 8\%$ (for 115 A beam current). The best measured phase stability of the TE_{31} amplified pulse was $\pm 10^\circ$ over a 9 ns period. The phase stability was limited because the maximum rf power was attained when operating far from wiggler resonance. The second harmonic, TE_{21} had a peak amplified power of 2 MW corresponding to 40 dB single-pass gain and 4% efficiency. The second harmonic interaction showed stronger superradiant emission than the third harmonic interaction. Characterizations of the second and third harmonic gyro-twt experiments presented here include measurement of far-field radiation patterns, gain and phase versus interaction length, phase stability, and output power versus input power.

This work was supported by the Department of Energy, Advanced Energy Projects Office, under contract number DE-FG02-89ER14052.

2 Introduction

High power microwave amplifiers in the millimeter and centimeter regime are needed for applications such as driving rf accelerators and beaming high power radiation into the atmosphere. Largely driven by demands for an rf source for the next generation of electron-positron accelerators and colliders, several high power microwave devices are currently under investigation at frequencies ranging from 3 GHz (SLAC klystrons) to 95 GHz (the atmospheric window) and beyond. Conventional microwave devices cannot deliver high power at high frequencies due to inherent scaling limitations. Because of this fundamental limitation, overmoded and harmonic devices such as the free electron laser and the gyrotron traveling-wave tube (gyro-twt) amplifier have generated a substantial amount of interest for providing high power, high frequency microwave sources.

Presented here are results from the first recorded multi-megawatt third harmonic gyro-twt as well as results from a multi-megawatt second harmonic gyro-twt. Strong strides have recently been made in harmonic gyro-devices. Very recently, a research group at the University of Maryland achieved 21 MW of output power with a second harmonic gyro-klystron amplifier[1], and later a UCLA

group achieved 200 kW rf output, 13% efficiency with a second harmonic gyro-twt[2]. Other significant gyro-twt results have been reported by groups at NTHU[3], NRL[4], Varian[5], and UCLA/UCD[2, 6]. The experiment from reference [4] in particular achieved 20 MW output power and 11% efficiency for a 60 ns pulse. A more detailed comparison of some of these experiments is shown on p. 20 of reference [7]. The gyro-twt has many promising features. It is relatively easy to build, has wide gain-bandwidth and high power capability, and is reasonably efficient. In addition, cyclotron autoresonance maser (CARM) and harmonic gyro-twt amplifiers can operate at high frequencies with relatively low magnetic field requirements. Finally, for a harmonic gyro-twt, as these experiments confirm, the higher the harmonic, the less prone the device is to instability[8].

3 Theory

The gyro-twt is driven by the well-known cyclotron resonance maser (CRM) interaction. CRM theory was developed in the late 1950's independently by several scientists[9, 10, 11], with many improvements having been added since then[12]–[22]. The CRM interaction is driven by electrons traveling helically in a uniform magnetic field. Randomly phased electrons first bunch together in velocity space both axially and azimuthally. The axial bunching is caused by non-relativistic effects and leads to the Weibel instability. In typical CRM devices, however, the azimuthal bunching, which is due to the (relativistic) negative mass instability, dominates the axial bunching[23] and leads to the CRM interaction, where the electrons emit radiation as they resonantly interact with a rotating TE wave.

The CRM resonance condition between the electrons and the wave is:

$$\omega = s\Omega_c + k_z v_z, \quad (1)$$

where ω and k_z are the frequency and axial wave number respectively, v_z is the axial electron velocity, $\Omega_c \equiv q_e B_0 / (m_0 \gamma)$ is the relativistic cyclotron frequency in the guiding magnetic field of amplitude B_0 , q_e is the unsigned charge of an electron, m_0 is the rest mass of an electron, and s is the harmonic number of the interaction. In the expression for Ω_c , γ is the normalized relativistic energy of the electrons: $\gamma = (1 - v^2/c^2)^{-1/2}$, where c is the speed of light in vacuum. Combining Eq. 1 with the dispersion equation for the relevant electromagnetic waveguide mode,

$$\omega^2 = c^2(k_\perp^2 + k_z^2), \quad (2)$$

yields the resonant radiation frequency. Here, k_\perp is the transverse wave number of a given waveguide structure, ck_\perp being the cut-off frequency of the structure. Eqs. 1 and 2 combine to form the cold CRM dispersion relation.

3.1 Nonlinear Equations

The nonlinear single particle equations of motion for the CRM interaction, neglecting space charge, have been derived by many authors: [24, 17, 15]

$$\frac{d\gamma_j}{d\hat{z}} = -\frac{q_e C_{mn}}{m_0 c \omega} J_{m-s}(k_\perp R_{gj}) J'_s(k_\perp r_{Lj}) \frac{\hat{p}_{\perp j}}{\hat{p}_{zj}} \operatorname{Re} \left\{ \tilde{E} e^{-i\Lambda_j} \right\}, \quad (3)$$

$$\begin{aligned} \frac{d\hat{p}_{zj}}{d\hat{z}} &= -\frac{q_e C_{mn}}{m_0 c \omega} J_{m-s}(k_\perp R_{gj}) J'_s(k_\perp r_{Lj}) \frac{\hat{p}_{\perp j}}{\hat{p}_{zj}} \left[\frac{1}{\beta_\phi} \operatorname{Re} \left\{ \tilde{E} e^{-i\Lambda_j} \right\} + \operatorname{Im} \left\{ \frac{d\tilde{E}}{d\hat{z}} e^{-i\Lambda_j} \right\} \right] \\ &\quad - \frac{\hat{p}_{\perp j}^2}{\hat{p}_{zj}} \frac{1}{2B_0} \frac{dB_0}{d\hat{z}}, \end{aligned} \quad (4)$$

$$\begin{aligned} \frac{d\Lambda_j}{d\hat{z}} &= \frac{\gamma_j}{\hat{p}_{zj}} - \frac{1}{\beta_\phi} - \frac{s\Omega_{c0}}{\omega \hat{p}_{zj}} - \frac{s^2 q_e C_{mn} J_{m-s}(k_\perp R_{gj}) J_s(k_\perp r_{Lj})}{m_0 c \omega k_\perp r_{Lj} \hat{p}_{zj} \hat{p}_{\perp j}} \\ &\quad \times \left[\left(\gamma_j - \frac{\hat{p}_{zj}}{\beta_\phi} \right) \operatorname{Im} \left\{ \tilde{E} e^{-i\Lambda_j} \right\} + \hat{p}_{zj} \operatorname{Re} \left\{ \frac{d\tilde{E}}{d\hat{z}} e^{-i\Lambda_j} \right\} \right], \end{aligned} \quad (5)$$

and

$$\begin{aligned} &\left[\frac{d^2}{d\hat{z}^2} + \frac{2i}{\beta_\phi} \frac{d}{d\hat{z}} - (1-i)(1-\beta_\phi^{-2}) \frac{\delta}{r_w} \right] \tilde{E} \\ &= \frac{2ik_\perp^2 C_{mn} I_0}{\omega \epsilon_0} \frac{1}{N} \sum_{j=1}^N J_{m-s}(k_\perp R_{gj}) J'_s(k_\perp r_{Lj}) \frac{\hat{p}_{\perp j}}{\hat{p}_{zj}} e^{i\Lambda_j}. \end{aligned} \quad (6)$$

In the above equations, γ_j is the relativistic energy factor of the j^{th} electron; $\hat{p}_{\perp j} \equiv \gamma_j v_{\perp j}/c$ is the normalized transverse momentum of the electron; $\hat{p}_{zj} \equiv \gamma_j v_{zj}/c$ is the normalized axial momentum of the electron; $\hat{z} \equiv \omega z/c$ is the normalized variable for z ; $\Omega_{c0} \equiv q_e B_0/m_0$ is the non-relativistic cyclotron frequency; R_{gj} is the guiding center of the j^{th} electron's orbit; $r_{Lj} = \frac{\gamma_j v_{\perp j}}{\Omega_{c0}} = \frac{\hat{p}_{\perp j} c}{\Omega_{c0}}$ is the Larmor radius of the electron's orbit; $k_\perp = \nu_{mn}/r_w$ for a circular waveguide; J_m and J'_m are the Bessel function of order m and its derivative; ν_{mn} is the n^{th} non-zero root of $J'_m(x)$; r_w is the circular waveguide radius; $\Lambda_j = \omega t_j - \hat{z}/\beta_\phi - s\phi_j + \pi/2$ is the relative phase between the electron and the rf-wave; $\phi_j = \tan^{-1}(v_{yj}/v_{xj})$ is the transverse velocity angle of the j^{th} electron; N is the number of particles; I_0 is the total electron beam current; ϵ_0 is the permittivity of free space; δ is the skin depth of the waveguide walls, which vanishes for a perfectly conducting wall; and $t_j(z) = t_j(z=0) + \int_{z'=0}^z \frac{dz'}{v_{zj}(z')}$ is the propagation time of a given particle, $t_j(z=0)$ differing for each particle and depending on the initial beam distribution.

In Eqs. 3–6, \tilde{E} , γ_j , \hat{p}_{zj} , $\hat{p}_{\perp j}$, Λ_j , Ω_{c0} , and B_0 are all implicitly functions of (and only of) \hat{z} . The parameter \tilde{E} is a complex quantity describing the amplitude and phase of the electric field of a TE_{mn} wave in a circular waveguide, m being the azimuthal index and n being the radial index; $\beta_\phi \equiv \omega/(ck_z)$ is the phase velocity of this wave; and $C_{mn} \equiv [J_m(\nu_{mn})\sqrt{\pi(\nu_{mn}^2 - m^2)}]^{-1}$ is a normalization factor so that the time-averaged power flowing through a cross-section of the waveguide is simply

$$\mathcal{P}(z) = \frac{1}{2k_\perp^2} \operatorname{Re} \left\{ \tilde{E}(z) \left[\frac{\tilde{E}^*(z)}{\eta_0 \beta_\phi} + \frac{i}{\mu_0 \omega} \frac{d\tilde{E}^*(z)}{dz} \right] \right\}. \quad (7)$$

where μ_0 is the permeability of free space, and $\eta_0 = \sqrt{\mu_0/\epsilon_0}$ is the impedance of free space. For the purposes of designing and analyzing these experiments, the code CRM32 was written to

numerically integrate an arbitrary number of particles through the gyro-twt interaction region using Eqs. 3–6. CRM32 loads the macro-particles with gaussian distributions in energy and momentum, and it has been well benchmarked against other existing CRM simulations.

4 Experimental Design

The experimental parameters chosen for the harmonic gyro-twt are based on beam parameters from SNOMAD II, a solid-state nonlinear magnetic-switching induction accelerator driver built by D. Birx of Science Research Laboratory[7]. A Pierce-gun geometry was used with SNOMAD II to generate a 400 kV, 300 A beam with a 30 ns flat-top. This same gun geometry and focusing system had been used in a previous klystron experiment with good success[25]. For the gyro-twt experiments, the axis-encircling beam from this gun geometry was spun-up by a three period bifilar helical wiggler electro-magnet. The wiggler causes the beam to corkscrew about the axis with an imparted pitch ($\alpha \equiv v_{\perp}/v_z$) near unity. The beam then flows through a region where the magnetic guide field tapers up to the gyro-twt interaction value, whereupon it interacts with an injected rf wave over a distance of ~ 1 –1.5 m. The amplified rf wave then exits through an output vacuum window into free space where it is measured by a detection system. A schematic for the experiment is shown in Fig. 1. The parameters chosen for the second and third harmonic gyro-twt experiments are shown in Table 1. The choice of waveguide mode in Table 1 is governed by the $J_{s-m}(k_{\perp}R_g)$ coupling parameter in Eqs. 3–6. Because the average guiding center radius, $\langle R_g \rangle$, of a Pierce-wiggler beam is zero, the strongest interacting mode for the second and third harmonics are the $m = s, n = 1$ modes: TE₂₁ and TE₃₁, respectively.

4.1 Beam Formation

The parameters in Table 1 were chosen based on an expected beam pitch of $\alpha \sim 1.0$. The beam formation is critical in determining the uniformity of the individual electron velocities within the beam. This, in turn, is critical to the expected efficiency of the gyro-twt, as demonstrated in Table 1. Note, however, that even with significant beam momentum and energy spreads ($\sigma_{p_z}/\langle p_z \rangle$ and $\sigma_{\gamma}/\langle \gamma \rangle$, respectively), the efficiency of the gyro-twt is still quite reasonable. This is not true in the case of a CARM amplifier, where sensitivity to beam spread is much greater. The reduced beam spread sensitivity of the gyro-twt was a significant factor in the choice of a harmonic gyro-twt for these experiments.

The beam quality for these experiments was determined largely by the wiggler. A wiggler form with a wiggler period of 9.21 cm was wound with 14 gauge (1.6 mm diameter) copper wire using 16 total passes. Transverse on-axis magnetic fields up to ~ 70 Gauss were measured using water cooling. Two computer models were used to simulate the effect of the wiggler magnet on the beam. The first is a simple single particle model that integrates a single electron through an ideal

Harmonic, s	2	3
Mode	TE ₂₁	TE ₃₁
Wall radius, r_w	9.525 mm	12.7 mm
Beam pitch, α	0.95	1.15
Axial Field, B_0	0.356 T	0.262 T
Gain-bandwidth (FWHM)	5.7 GHz	4.0 GHz
$\sigma_\gamma/\langle\gamma\rangle = 0\%$, $\sigma_{pz}/\langle p_z\rangle = 0\%$		
Efficiency, η	19.4%	17.7%
Power	27.2 MW	24.7 MW
Gain	54.4 dB	53.9 dB
Saturation length, z_{SAT}	0.53 m	0.88 m
$\sigma_\gamma/\langle\gamma\rangle = 2\%$, $\sigma_{pz}/\langle p_z\rangle = 10\%$		
Efficiency, η	6.4%	6.0%
Power	9.0 MW	8.4 MW
Gain	49.5 dB	49.3 dB
Saturation length, z_{SAT}	0.63 m	0.77 m

Table 1: Final design parameters for the CARM and gyro-twt experiments. Each case corresponds to parameters near the optimal efficiency for each harmonic. Parameters that the experiments have in common are frequency, $f = 17.136$ GHz, beam voltage, $V = 400$ kV, beam current, $I = 350$ A, and rf drive power, $P_{IN} = 100$ W. The overall efficiencies were calculated by CRM32 using $N = 4096$ and a 1.2 cm wide top-hat distribution in guiding-center radius.

transverse rotating magnetic field using the following two equations[7]:

$$\frac{dp_{\perp}}{dz} = q_e B_w \sin(k_w z - \phi) \quad (8)$$

$$\frac{d\phi}{dz} = q_e \left[\frac{B_z}{p_z} - \frac{B_w}{p_{\perp}} \cos(k_w z - \phi) \right], \quad (9)$$

where B_w is the transverse on-axis magnetic field, $k_w = 2\pi/\lambda_w$, λ_w is the wiggler period or wavelength, B_z is the axial on-axis magnetic field, and $\phi = \tan^{-1}(v_y/v_x)$. At one particular axial guide field strength (for all other parameters fixed), a maximum transverse momentum will be imparted to the beam. This condition is referred to as ‘‘wiggler resonance.’’ One can operate the experiment with the guide field above or below this resonance point, and this operational setting turns out to be an important factor in determining beam quality. After passing through the wiggler region, the axial guide magnetic field strength is adiabatically increased from the value in the wiggler region to the value necessary for the gyro-twt interaction. The compression region is typically 15–25 cm in length for these experiments.

A second, multiple particle simulation was also used to model the wiggler. Because the beam path is not axisymmetric, the MIT TRAJ code[26, 27, 28] was written to integrate multiple particles through fully 3D trajectories. TRAJ also tracks the particles after the wiggler exit and through the region of adiabatic magnetic field compression. TRAJ includes the effects of transverse self-fields (electric and magnetic), but does not include axial self-fields due to inherent limitations in the model. For the design parameters listed in Table 1, TRAJ predicts axial momentum spreads of 5–7%.

4.2 Magnetic Tapering

The output powers and efficiencies shown in Table 1 were calculated using a uniform (in z) axial magnetic guide field. Several authors have shown[20, 18, 19] that an appropriate taper in the magnetic field just before the saturation point of the rf wave can lead to significantly increased efficiency. As the electrons lose energy to the wave in a gyro-twt, γ will decrease, causing the relativistic cyclotron frequency, Ω_c , to increase. For a gyro-twt this is the dominant change in the resonance condition as the electrons lose energy (see Eq. 1). For a CARM, the $k_z v_z$ term also decreases, tending to offset the increase in Ω_c , hence autoresonance. Since the gyro-twt is not autoresonant, down-tapering the magnetic field, thereby keeping the relativistic cyclotron frequency constant as the particles lose energy, can be used to maintain resonance, which results in higher efficiency. Under certain conditions, an uptaper also can improve efficiency because it pumps more transverse velocity into the beam, which increases the beam-wave coupling. The optimal taper typically begins just before saturation and has a down-slope of $0.04\Gamma B_0$ – $0.08\Gamma B_0$, where Γ is the electric field growth rate of the gyro-twt interaction, $E \propto e^{\Gamma z}$ [18]. A specific design for a magnetic field taper is not critical for the gyro-twt design process. Rather, the enhanced efficiency that results from tapering is a motivation to design the interaction field magnet system so that the field can be easily tapered.

4.3 Experimental Components

The beam diagnostics flange used in the experiment (immediately preceding the rf input coupler in Fig. 1) provides signals from a diamagnetic loop and four “b-dot” loops. The diamagnetic loop is oriented so that the beam passes directly through it, thus generating a signal correlated to the time-changing pitch of the beam. The b-dot loops have surfaces oriented parallel to the z -axis, rotated around the beam at 0, 90, 180, and 270 degrees. These loops measure the time-changing azimuthal B-field, which is proportional to the beam current. Using careful calibration, they provide accurate information as to beam current and centering. The diamagnetic loop proved too difficult to calibrate for precise beam pitch measurements, but the traces do reveal the qualitative shape of the beam pitch profile in time, and such traces are useful for viewing the occurrence of wiggler resonance.

The rf-input coupler for the experiments is a rectangular WR-62 waveguide brazed perpendicularly to a cylindrical waveguide with a very light wire mesh placed inside the circular guide at 45° to bounce the incoming rf from the WR-62 guide into the circular guide. Input rf was provided by a 17 GHz, 60 kW magnetron. The magnetron signal, propagating at 17.1 GHz in WR62 waveguide, is single-moded in the TE_{10} mode. The WR62 in-guide signal strength was measured through a nominal -60 dB broadwall coupler. The signal was then directed through an isolator and into the gyro-twt input coupler, which couples the WR-62 TE_{10} mode to circular fixed waveguide modes. The mesh in the input coupler quickly developed a small hole in the center due to the electron beam. The rf input coupler (with hole in mesh) was well characterized during cold tests using far field radiation patterns, coupling significant power to the fixed TE_{11} ($\sim 15\%$), TE_{21} ($\sim 80\%$), and TE_{31} ($\sim 5\%$) modes. For our experimental set-up with an axis-encircling beam in a circular guide, only half the power in a fixed mode couples to the appropriate gyro-twt rotating mode. The output waveguide section provides a waveguide radius uptaper from the interaction radius to 2.54 cm in order to avoid possible breakdown and provide a better match to free space. The vacuum window is made of alumina ceramic ($\epsilon = 9.6\epsilon_0$) and is 1.43 cm thick, matched at 17.1 GHz. The emitted rf was measured by a WR-42 detecting horn, attenuator, and diode in the far field region. The horn was constrained to pivot about the radiating aperture in the horizontal plane, moved by a 2D, computer-controlled scanning table. In all, the gyro-twt experiments, as shown in Fig. 1, were each approximately 3 meters in length. The experimental setups are discussed in much greater detail in [7].

5 Experimental Results

The voltage pulse of SNOMAD-II is measured from a capacitive probe next to the bus bar of the linac. All signals from these experiments were recorded using a high speed (up to 2 GS/sec) digital storage oscilloscope. A typical SNOMAD-II shot is shown in Fig. 2, with the time-integrated b-dot signal resulting from the linac current pulse overlaid on top of a current-viewing resistor (CVR) signal from the same pulse. The CVR signal is used to calibrate the b-dot signal. The CVR was in place during preliminary experiments to study the beam and measured current returned beam collector.

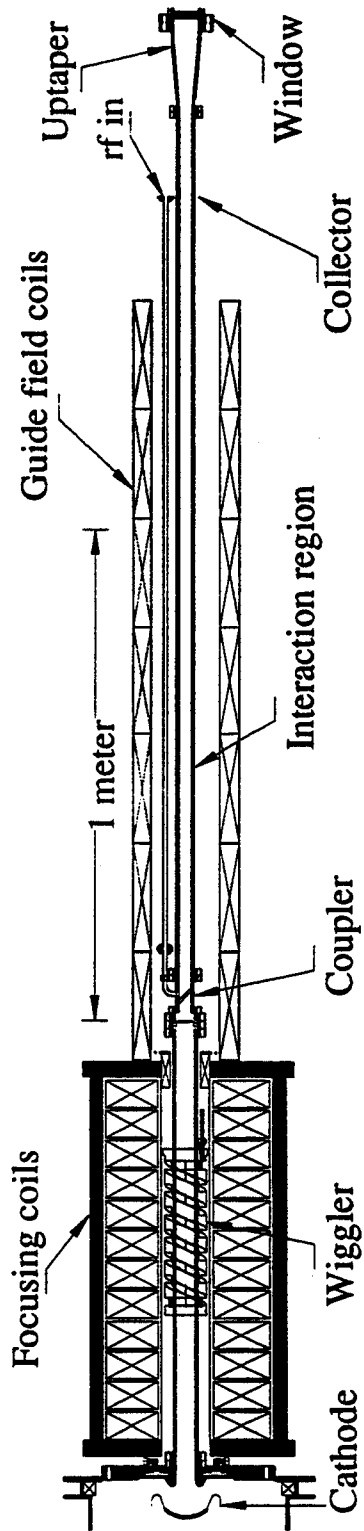


Figure 1: A 1:15 scale drawing of the entire gyro-twt experiment.

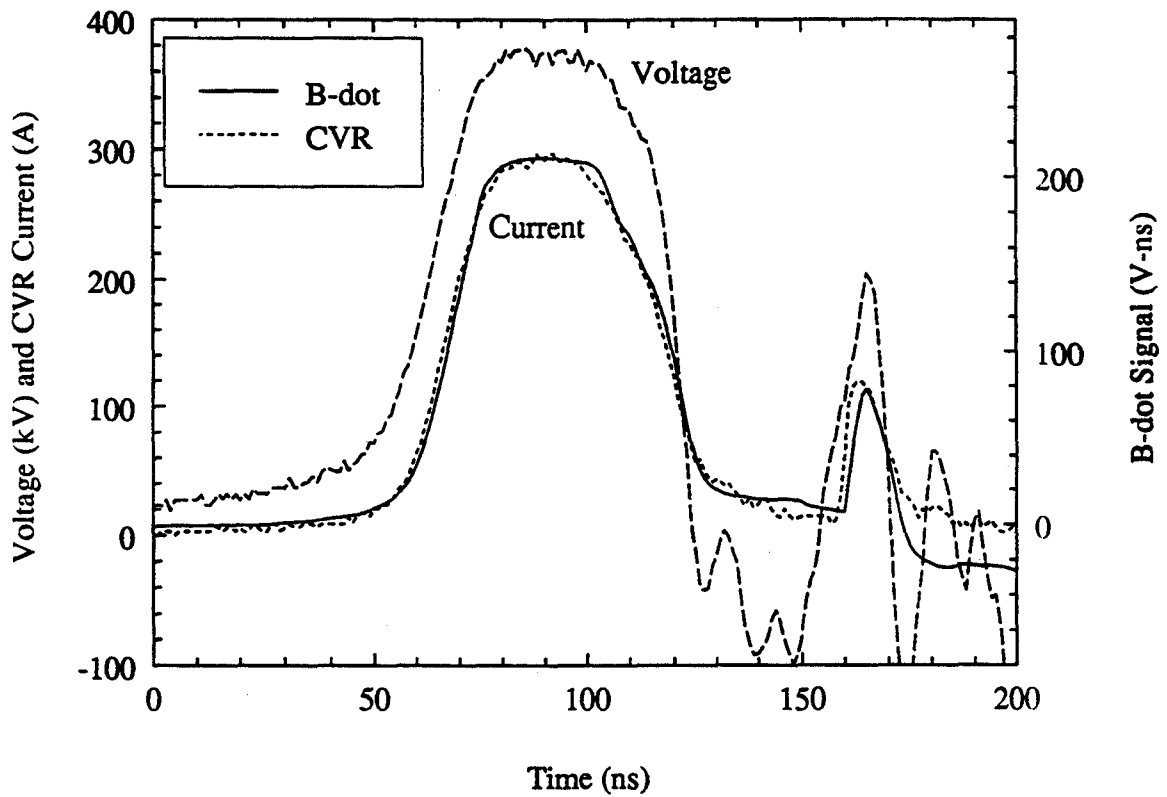


Figure 2: B-dot signal (time-integrated) with CVR signal and voltage pulse overlaid. The b-dot signal and the CVR signal are both proportional to beam current.

For verification of correct wiggler operation, the CVR trace was monitored while the axial guide field of the focusing coils was tuned. At wiggler resonance, with the wiggler field set high enough, some of the beam current spills to the beam tunnel before reaching the CVR, and the CVR trace shows a marked decrease during this resonance. This condition was used to experimentally determine the wiggler guide field settings that were resonant with various beam voltages, and the results are shown in Fig. 3. They match the simple theory prediction quite well.

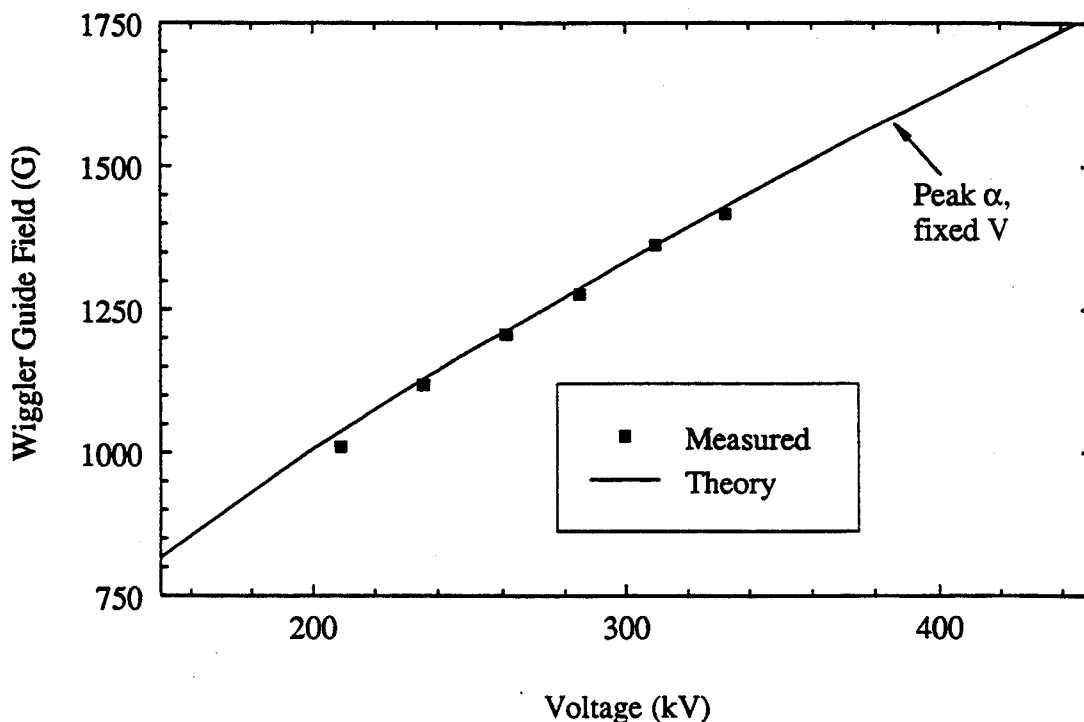


Figure 3: Theoretical and measured wiggler resonance points. The solid curve shows the theoretical peak in beam pitch, α . This same line corresponds to peaks in the Larmor radius of the beam, r_L . The theory was calculated from Eqs. 8 and 9. The measured values (filled squares) were obtained by tuning the guide field at a fixed voltage in each case until the beam current trace showed maximum current loss. The measured voltage values are adjusted by -5% from the capacitive probe reading to account for beam voltage depression. The on-axis transverse wiggler field was set to 50 G for these measurements.

5.1 Cold Tests

The performance of the gyro-twt rf input coupler was measured primarily by analysis of the far-field radiation pattern emitted from the gyro-twt window, just as the amplified gyro-twt signal was also characterized. In the absence of an electron beam, the magnetron was pulsed at 1 Hz. The waveguide horn in the far-field region, depending on its orientation, detected either the vertical or the horizontal polarization of the E-field in the emitted rf wave. Letting z be the beam axis, x be

the horizontal axis, and y be the vertical axis, and defining $r = \sqrt{x^2 + y^2}$, $\theta \equiv \cos^{-1}(z/r)$, and $\phi \equiv \tan^{-1}(y/x)$, then the two measured polarizations of the E-field are E_θ and E_ϕ . The far-field limit solution of the well known Stratton-Chu equation for radiation from a circular aperture is[29]

$$\begin{aligned} E_\theta &= (-i)^m \sqrt{\frac{\mathcal{P}}{2\eta_0\beta_\phi}} \frac{C_{mn} m \omega \mu_0}{k_z} \frac{e^{-ik_f r}}{r} e^{-im\phi} \left(1 + \frac{k_z \cos \theta}{k_f}\right) \frac{J_m(\nu_{mn}) J_m(k_f r_w \sin \theta)}{\sin \theta} \\ E_\phi &= (-i)^{m+1} \sqrt{\frac{\mathcal{P}}{2\eta_0\beta_\phi}} \frac{C_{mn} k_\perp^2 r_w \omega \mu_0}{k_z} \frac{e^{-ik_f r}}{r} e^{-im\phi} \frac{J_m(\nu_{mn}) J'_m(k_f r_w \sin \theta)}{k_z - k_f \cos \theta}, \end{aligned} \quad (10)$$

where the notation is the same as in Eqs. 3–7 except that here r and ϕ are observation point coordinates and not waveguide coordinates, and r_w is the aperture radius. The match between Stratton-Chu and the far field approximation is very good for the frequency, aperture size, and horn distance used in these experiments. In general, the far-field criterion is $r > 2D^2/\lambda$, where r is the distance from the aperture to the horn, D is the aperture diameter, and λ is the free space wavelength.

A computer program was written that matches an arbitrary measured far field radiation pattern to the theoretical pattern (from Eq. 10) resulting from a mix of a finite number of waveguide modes. The user selects the desired number of modes, and each mode selected for inclusion in the pattern matching is allowed to have an arbitrary phase and an arbitrary amplitude. The program searches through the parameter space of different phases and amplitudes for each mode using Powell's search algorithm[30] to quickly find a mode mix giving a best fit to the measured data. The program that finds this best fit is called FFMATCH, and it was written specifically for these experiments. The absolute power of the rf pulse is also predicted by FFMATCH by having it predict the total in-guide power in each mode necessary to match the intensity pattern measured by the far-field horn. This power estimate is dependent on the mix of modes chosen and is also critically dependent on accurate measurement of the rf intensity by the detecting horn.

The power estimated by the FFMATCH program is adjusted in one critical way. The following calculation is performed numerically on the far field radiation pattern for each different mode:

$$\mathcal{P}_R = \frac{1}{2\eta_0} \int_0^{\pi/2} \int_0^{2\pi} (|E_\phi|^2 + |E_\theta|^2) r \sin \theta d\phi d\theta, \quad (11)$$

where E_ϕ and E_θ are from Eq. 10, \mathcal{P}_R represents the total radiated power from the mode, and the integral is over the entire forward hemisphere ($z > 0$) of the radiating aperture. For the radiation patterns predicted by Eq. 10 for the gyro-twt parameters, the value of \mathcal{P}_R from Eq. 11 for modes other than the TE₁₁ mode is significantly less than the power assumed to be in the waveguide. That is, the radiated patterns do not conserve power for the gyro-twt radiation parameters. With 1 W in waveguide for the TE₂₁ mode, $\mathcal{P}_R = 0.85$ W. With 1 W in waveguide for the TE₃₁ mode, $\mathcal{P}_R = 0.81$ W. This error is inherent in Eq. 10 for the gyro-twt operating parameters. The error is partly due to the Stratton-Chu theory assuming unperturbed waveguide fields at the emitting aperture when in fact edge currents at the aperture are not taken into account, resulting in an underprediction of power in the far field. A detailed discussion of this underprediction is found in reference [31], Ch 4. The FFMATCH program compensates for the underprediction by forcing

power to be conserved by artificially increasing the intensity of the far field radiation patterns for the TE_{21} and TE_{31} modes by $1/0.85$ and $1/0.81$, respectively. In the far field power predictions made by FFMATCH, this adjustment is taken into account.

The first example of a match from FFMATCH is a calibration measurement shown in Fig. 4, where a TE_{31} mode of a known power level was radiated into the far-field measurement system and matched with FFMATCH. The mode was generated from a TE_{10} mode in WR-62 passing through a rectangular-to-circular converter, a fixed-to-rotating converter, and a rippled-wall TE_{11} -to- TE_{31} converter[32]. Together, all of the converters are $> 90\%$ efficient. The power prediction

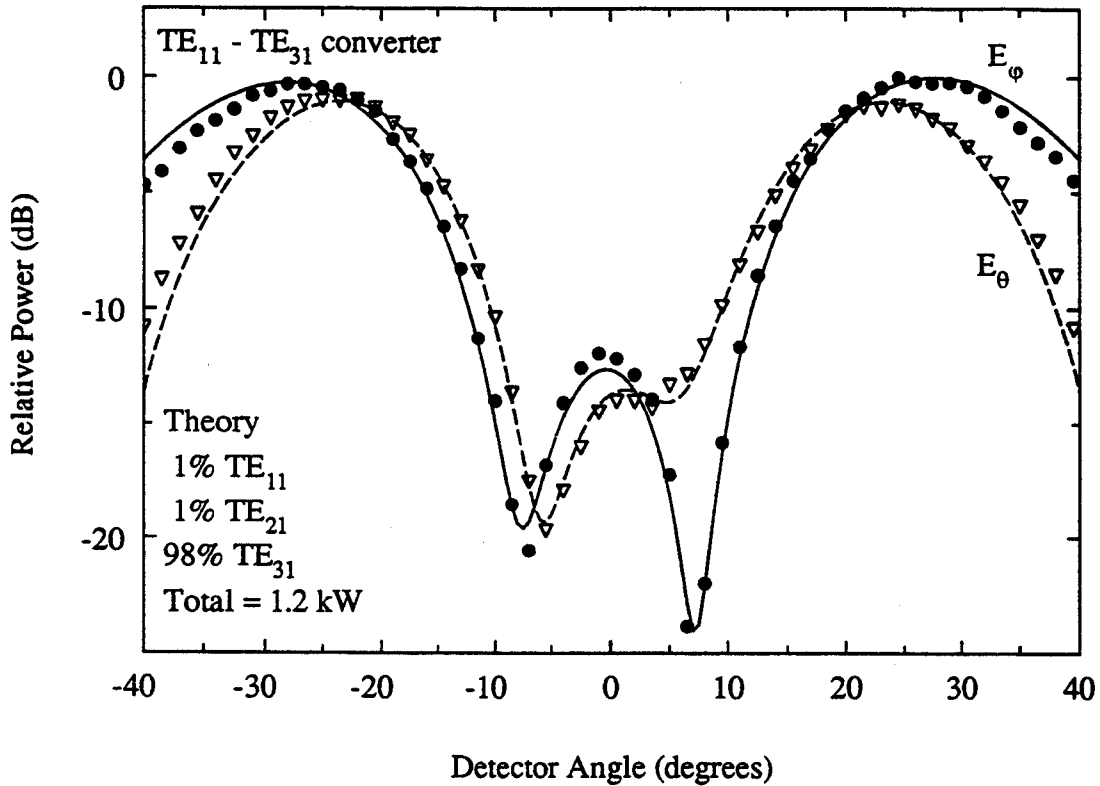


Figure 4: Calibration of far field power prediction for TE_{31} mode. A TE_{31} wave of known power was launched from the gyro-twt window and measured in the far field. The FFMATCH program was then used to predict the total launched power based on the measured radiation pattern. The filled circles show measurement of E_ϕ , and the open triangles show measurement of E_θ . Each measured value is an average over several magnetron pulses. The curves are theory results from the FFMATCH predicted mode mix. The actual power launched was 0.8 kW, and FFMATCH predicts 1.2 kW. This is a difference of 1.8 dB.

by FFMATCH is 1.8 dB higher than the power prediction from the in-guide power measurement, which was done using a broadwall coupler on the WR-62 guide and a well calibrated rf diode. Based on the VSWR of each component involved in the rf power measurement and also based on the result shown in Fig. 4, the error bar for the power predictions for these experiments is considered to be ± 2 dB.

5.2 Gyro-twt Power and Gain Measurements

During the majority of the gyro-twt experimental operation (August 1991–March 1994), the third harmonic, TE₃₁ interaction tube was in place, hence the TE₃₁ mode measurements are more complete, and the amplifier operation in that mode is better characterized. Table 2 summarizes four run settings where a fairly complete characterization of the amplifier operation was performed, including far field scans, power measurements, gain measurements versus interaction length, and phase and spectral measurements on the amplified pulse.

Case	A	B	C	D
Harmonic, s	3	3	2	3
Mode	TE ₃₁	TE ₃₁	TE ₂₁	TE ₃₁
Voltage, V	385 kV	380 kV	320 kV	370 kV
Current, I	300 A	160 A	130 A	150 A
Frequency, f	17.1 GHz	17.1 GHz	17.1 GHz	17.1 GHz
Wall radius, r_w	12.7 mm	12.7 mm	9.525 mm	12.7 mm
Wiggler field, B_w	65 G	65 G	25 G	60 G
Wiggler guide field, B_{wz}	1830 G	1865 G	1490 G	1780 G
Resonant wiggler guide field	1560 G	1550 G	1480 G	1525 G
Beam pitch, α (theory)	0.65	0.6	0.55	0.6
Interaction Field, B_0	0.28 T	0.27 T	0.35 T	0.27 T
Input Power	1200 W	30 W	200 W	200 W
Power	4 MW	4 MW	2 MW	3 MW
Efficiency, η	3.5%	6.5%	4%	5%
Gain	35 dB	51 dB	40 dB	42 dB
Growth rate	1.0 dB/cm	1.0 dB/cm	0.7 dB/cm	0.9 dB/cm
Saturation length, z_{SAT}	0.84 m	1.1 m	0.95 m	0.95 m
Superradiant signal level	-15 dBc	-40 dBc	-10 dBc	-40 dBc

Table 2: A list of run parameters and measured gain and power for four different cases: High current, low gain TE₃₁ (A), Low current, high gain TE₃₁ (B), low current, moderate gain TE₂₁ (C), and low current, moderate gain TE₃₁ (D). The interaction field was tapered in each case, so the B_0 value is an approximate value. The beam pitch value is predicted by Eqs. 8 and 9. The input power, output power, gain, and efficiency are all based on far field measurements and have ± 2 dB error bars. The frequency in each case is 17.1 GHz.

Fig. 5 shows amplified rf pulses from third harmonic, TE₃₁ (top) and second harmonic, TE₂₁

(bottom) interactions. In general, the amplified power was quite stable, the changes in diode traces from shot-to-shot at times being imperceptible to the naked eye. This stability allowed for thorough measurements which could be taken over thousands of shots at a 1 Hz pulse rate. The amplified traces, as expected for gyro-twt operation, were only present when both the wiggler and the magnetron were turned on. With the injected rf drive signal not present, the gyro-twt output level was anywhere from 10 dB (TE_{21}) to > 40 dB (TE_{31}) lower than for the amplified signal (see Table 2, superradiant signal level). The frequency of the rf pulses was verified by passing them through a 350 MHz bandwidth YIG-tuned filter centered at 17.1 GHz. The superradiant mode (emitted with rf drive off), typically had a frequency in the range 16.6–16.9 GHz, and the radiation pattern was typically the same as the amplified pattern, but it was not reproducible enough shot-to-shot to measure accurately.

As already mentioned, power and gain measurements were made using calibrated diodes and matching to the measured far-field radiation patterns using the FFMATCH program. Two such matches are shown in Fig. 6 for a third harmonic (top) and second harmonic (bottom) amplified pulse. These results correspond most closely to the Case D and C run parameters listed in Table 2. The gyro-twt performed more efficiently at lower beam currents. The beam current for any given run was affected by several factors, including degrading cathode performance over time (e.g. time extending over months of use and multiple vacuum breaks), vacuum conditions, and cathode heater setting.

The gain “history,” or gain versus interaction length, for the TE_{31} (top) and TE_{21} (bottom) interactions is shown in Fig. 7. The measurement was made by sliding a pair of “kicker” magnets along the length of the interaction tube. The strong transverse field from the kicker magnets deflects the electron beam into the wall of the interaction tube, causing the gyro-twt interaction to cease. The detector horn was kept at a fixed angle in the radiation pattern (where the pattern peaked), and the measured rf pulse amplitude was averaged over several shots for each data point. All measured values are then normalized to the power predicted by the integrated far field radiation pattern. A good theoretical match to the gain curves, using the CRM32 code with $N = 4096$ particles, is consistently obtained when using a beam pitch of $\alpha \sim 0.9$, an axial momentum spread of $\sim 12\%$, and a beam energy spread of $\sim 3\%$.

5.3 Frequency and Phase Measurements

The TE_{21} amplified pulses tended to be wider than the TE_{31} pulses, but they also had significant frequency variation, or chirping. A phase discriminator (Anaren #20759) was added to the experimental setup towards the end of the experiment in order to measure the time-profile of the phase of the rf pulses. The discriminator was only in place for third harmonic, TE_{31} operation. The phase measurements shown in the top graph of Fig. 7 were taken using the phase discriminator. For full spectral analysis of a pulse, three separate techniques, all giving consistent results, were used: measuring the phase with the phase discriminator; mixing the amplified rf signal with a known frequency to generate an intermediate frequency (I.F.) signal; and using a narrow (40 MHz) bandwidth YIG-tuned filter. Results from the phase discriminator and the mixer are shown in Fig. 8

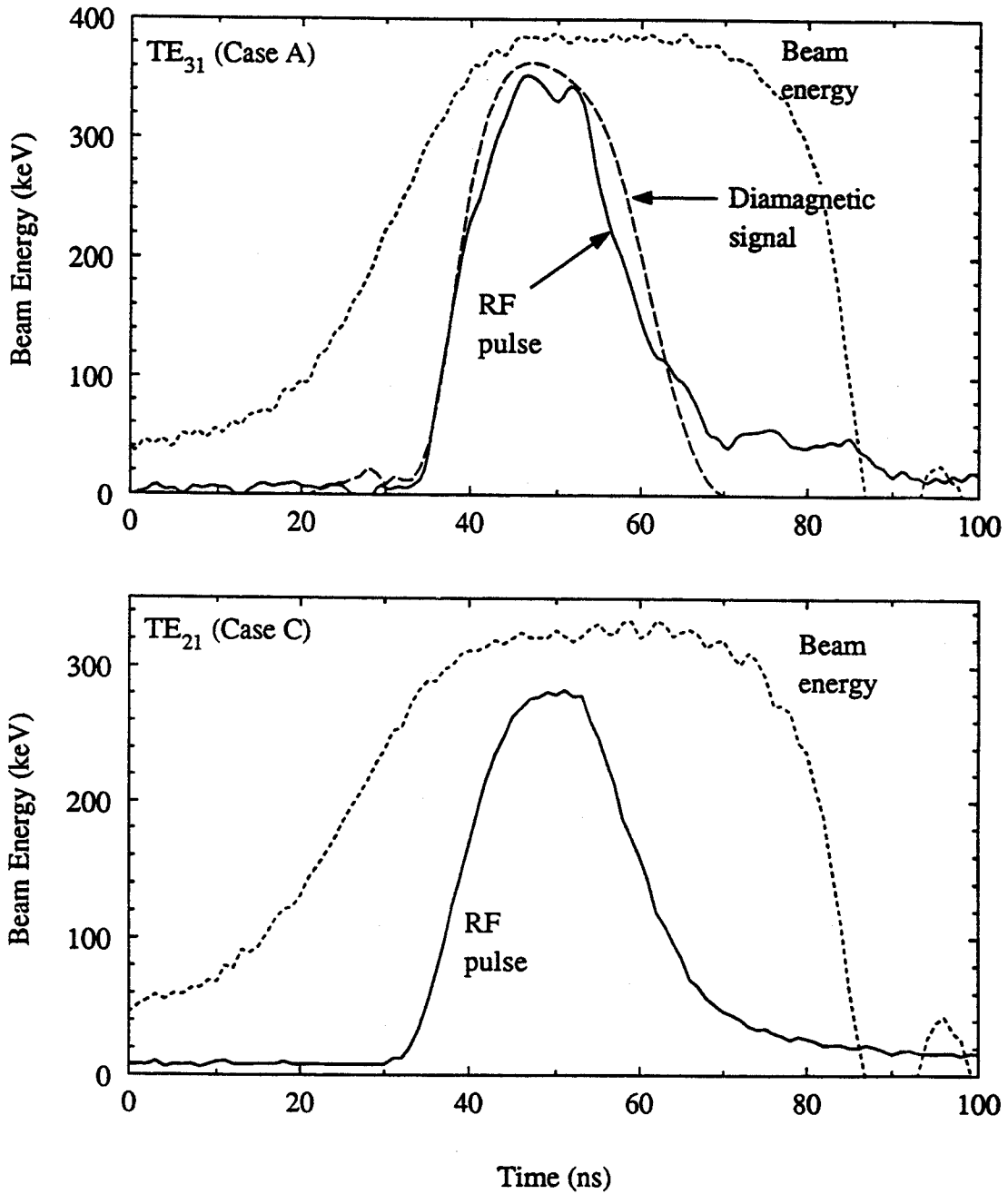


Figure 5: The top figure shows a voltage pulse, a time-integrated diamagnetic loop pulse, and an amplified TE₃₁ rf pulse from Case A in Table 2. The rf pulse, proportional to the diode signal, and the diamagnetic loop signal, proportional to V·s, are in arbitrary units. The bottom figure shows a voltage pulse and an amplified TE₂₁ rf pulse from Case C.

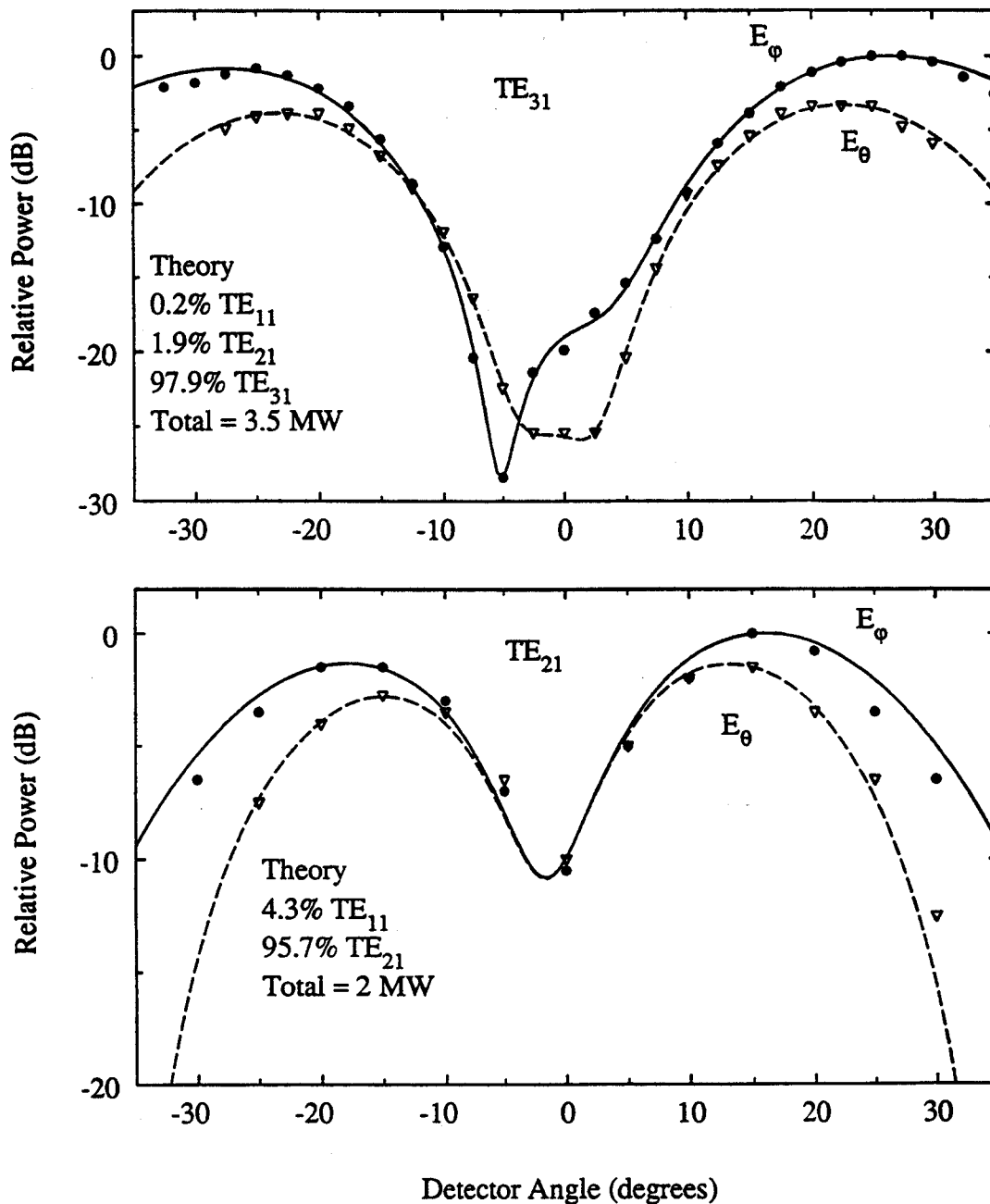


Figure 6: Measured and best-fit TE₃₁ (top) and TE₂₁ (bottom) radiation patterns from run parameters similar to cases D and C, respectively, in Table 2. The TE₃₁ case with a beam voltage and current of 380 kV and 115 A, corresponds to an efficiency of 8%. The filled circles show measurement of E_ϕ , and the open triangles show measurement of E_θ . Each measured value is an average over several gyro-twt pulses. The mode mix and total power corresponding to the theory curves are calculated by the FFMATCH program.

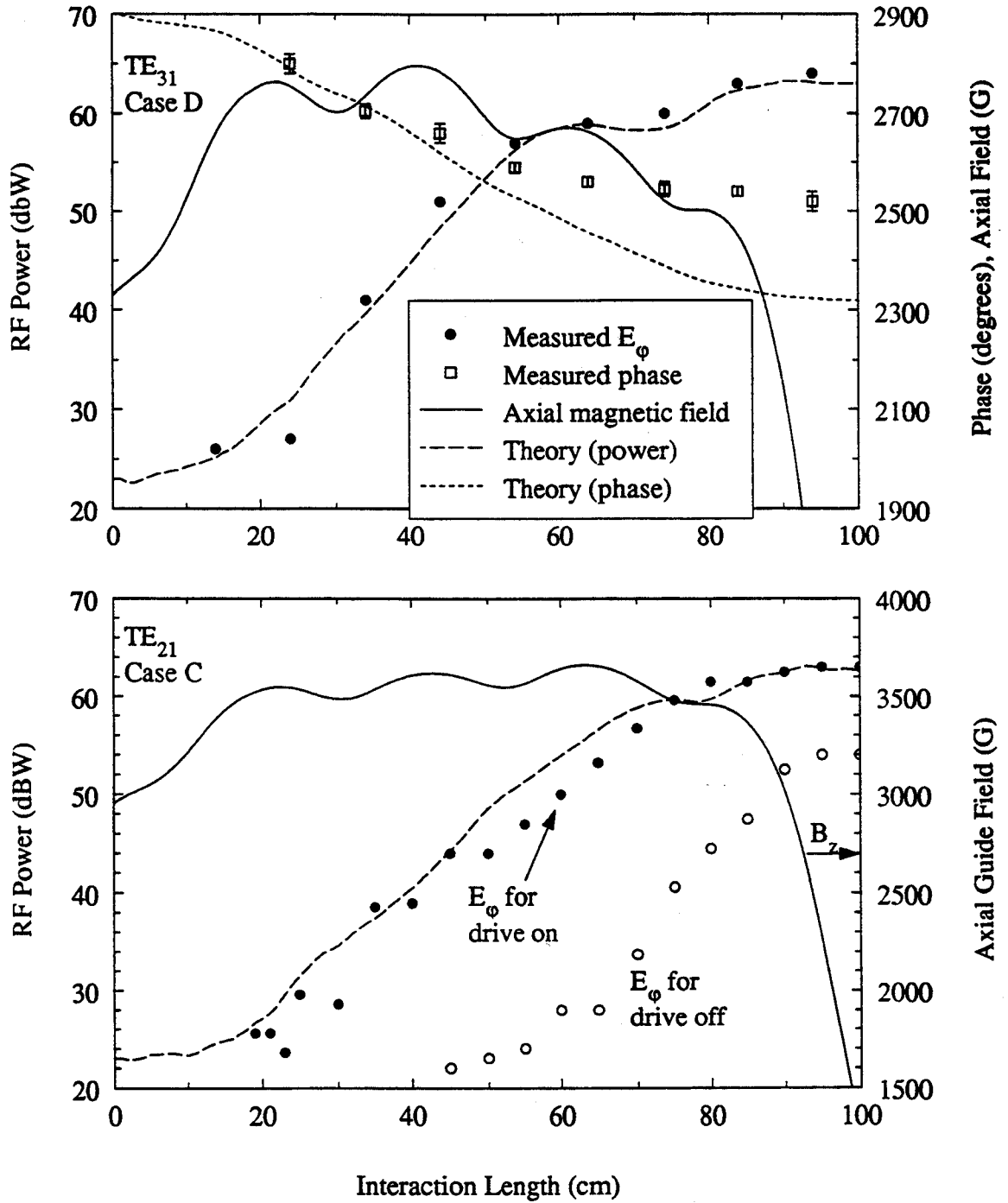


Figure 7: Measured and theoretical TE₃₁ amplified rf power and phase (top) and TE₂₁ amplified rf power and superradiant power (bottom) plotted against gyro-twt interaction length. The plots are from Cases D and C from Table 2. The peak measured powers are 3 MW (top) and 2 MW (bottom) with ± 2 dB absolute error and ± 0.5 dB relative error. The filled circles represent the amplified signal level, the open squares represent the measured phase, and the open circles represent superradiant signal level. Since the absolute phase is arbitrary, the magnetic field axis was also used for the phase, except in degrees rather than Gauss. The theory curves in each case are generated by CRM32 with $N = 4096$ particles, a beam radius of 5 mm, and initial values of $\alpha = 0.9$, $\sigma_\gamma / \langle \sigma_\gamma \rangle = 3\%$, and $\sigma_{p_z} / \langle p_z \rangle = 12\%$.

for a typical TE₃₁ pulse (Case D). The measured phase variation shown in Fig. 8 (bottom), when fit to a parabola, yields the straight-line frequency chirp shown in the top plot of Fig. 8. This chirp of ~ 8 MHz/ns agrees well with the chirp predicted by the zero-crossing frequencies of the I.F. signal. The zero-crossing frequencies and the I.F. signal are shown in Fig. 8 (top).

Note that the diamagnetic loop time-integrated pulse in Fig. 8 has a similar parabolic shape to the measured phase of the rf pulse. Assuming that the diamagnetic loop signal scales like the square of the transverse velocity of the beam (β_{\perp}^2), which is reasonable for small beam pitch, and also assuming that the beam pitch is $\alpha = 0.6$, a parabola is fit to the diamagnetic loop pulse in Fig. 8 over the range of phase shown in the figure. The fit, given the assumptions, results in the following time profile of β_{\perp} near the peak of the pulse:

$$\beta_{\perp} \approx \beta_{\perp\text{MAX}} - 0.0015\beta_{\perp\text{MAX}} \left(\frac{t}{1 \text{ ns}} \right)^2 \quad (12)$$

If it is then assumed that $\phi(t)$ changes 5°/% for changes in β_{\perp} (a value predicted by CRM32 for this case), the phase variation resulting from Eq. 12 would be (for all other parameters fixed)

$$\phi(t) \approx \phi_{\text{MAX}} - 0.75^{\circ} \left(\frac{t}{1 \text{ ns}} \right)^2 \quad (13)$$

The resulting frequency chirp is $1.5^{\circ}/\text{ns}^2 = 4$ MHz/ns. Though the calculation is very simplified, it results in a chirp value of the same order as the measured 8–10 MHz/ns chirps. It should be noted that the voltage variation during the time when the phase variation was measured is much less significant than the diamagnetic loop variation. A fit to the voltage pulse yields $V(t) \approx V_{\text{MAX}} - 0.0004V_{\text{MAX}}(t/1 \text{ ns})^2$. The highly parabolic shape of the beam pitch profile appears to have been the limiting factor in the gyro-twt phase stability. Two of the best results in phase stability for the TE₃₁ case, as measured by the phase discriminator, are $\pm 20^{\circ}$ over 15 ns and $\pm 10^{\circ}$ over 9 ns. These measurements were made at a predicted rf power level of 3 MW.

5.4 In-Guide Power and Other Measurements

For the final six months of experimental operation, an rf gun transmission line was attached to the output of the gyro-twt, and the gyro-twt was operated in the third harmonic, TE₃₁ mode. This involved removing the gyro-twt output window and appending a 2 m section of 5.08 cm I.D. circular waveguide to the gyro-twt uptaper. This large section of waveguide is followed, in order, by a downtaper to 2.54 cm I.D., a rippled-wall TE₃₁-to-TE₁₁ converter, an elliptical TE₁₁ rotating-to-TE₁₁ fixed mode converter, a circular-to-rectangular transition, a -60 dB forward wave pickoff coupler, and finally the rf gun itself. This hardware all constituted the rf gun transmission line[32]. Many of the parts were the same used in the calibration discussed in Sec. 5.1. The 2 m section was used to provide isolation distance between the rf gun and the gyro-twt. The rf transmission line allowed for an in-guide measurement of the rf power based on calibrated diode detection at the -60 dB coupler. The peak rf power of amplified pulses using the rf gun transmission line was ~ 2.5 MW at parameter settings consistent with the high power TE₃₁ measurements from Case D

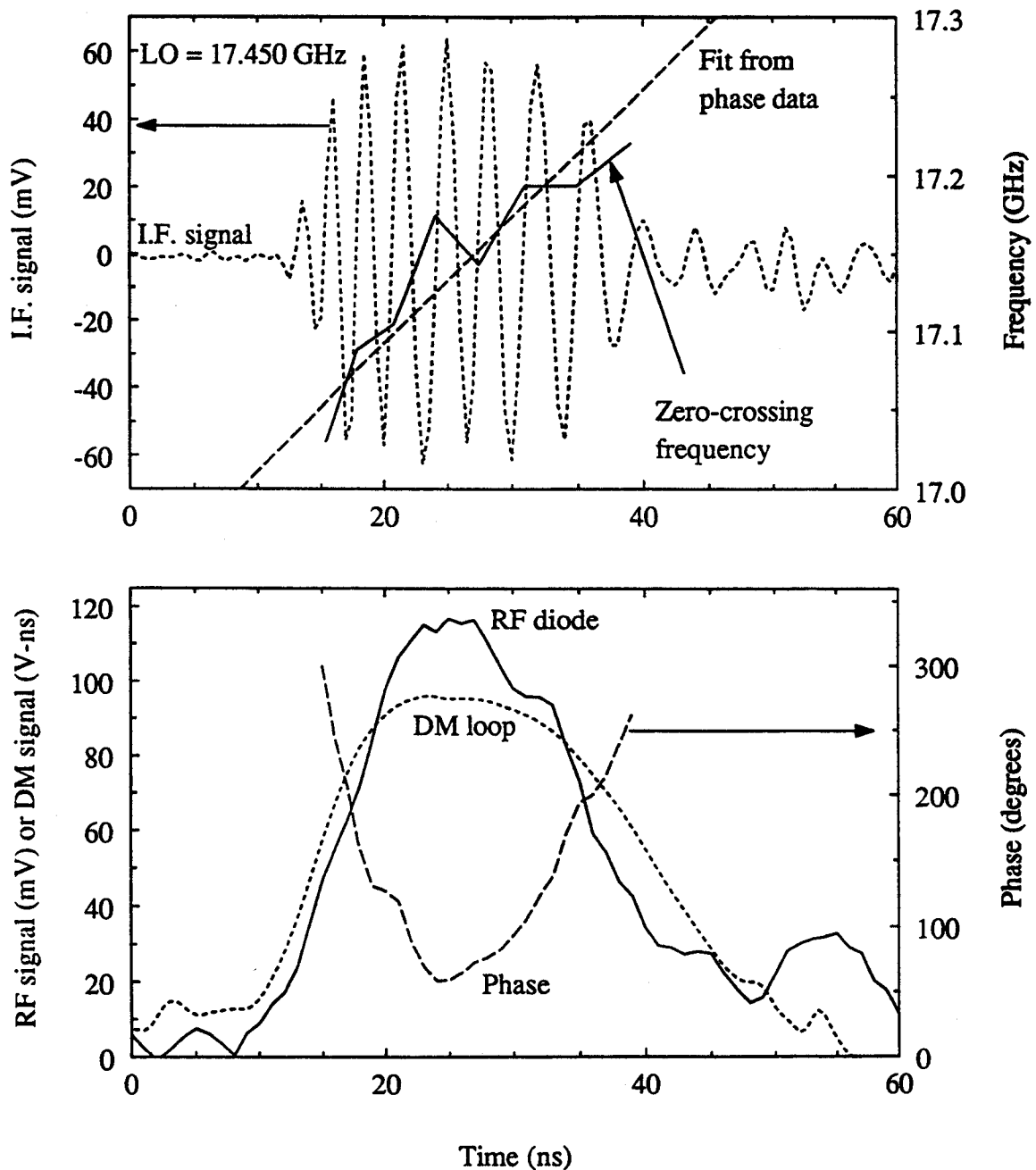


Figure 8: Phase variation and frequency chirp measured on a high power TE_{31} pulse. The top figure shows the I.F. signal (dashed curve) for a ~ 3 MW amplified TE_{31} gyro-twt pulse mixed with a 17.45 GHz local oscillator. This pulse is from Case D in Table 2. The bottom figure shows the actual rf pulse, its measured phase variation using a phase discriminator, and a diamagnetic loop time-integrated pulse. A parabola was fit to the phase signal in the bottom figure and then differentiated to get the straight line in the top figure, which predicts the frequency chirp of the rf pulse. For comparison, the zero-crossing frequency is also shown on the top figure.

in Table 2. Considering that the estimated transmission line loss is ~ 1 dB, this value corresponds to ~ 3 MW, which is in good agreement with the far field power measurements that were made just previous to installing the rf gun transmission line.

Just before the termination of the gyro-twt experiments, in early March, 1994, a side-wall hole coupler replaced the wire-mesh input coupler of the gyro-twt. The side-wall coupler couples rectangular TE_{10} radiation from WR62 guide into TE_{31} radiation in 2.54 cm I.D. circular guide. The measured coupling from this input coupler was substantially better than the wire-mesh coupler for the TE_{31} mode; however, it was not characterized in the far field due to time constraints. In addition, no improvement in gyro-twt performance was measured due to the installation of the new coupler. It was expected that removing the wire-mesh from the beam path might improve the quality of the electron beam; however, the beam did partially destroy the mesh in the original coupler, vaporizing the center portion with a hole diameter of ~ 1 cm.

The components of the gyro-twt experiments were not designed for wide bandwidth. The input coupler and the output window are narrow band components, and the magnetron used to drive the gyro-twt experiments has limited frequency range. This made accurate measurement of the gain-bandwidth of the gyro-twt experiments infeasible.

6 Discussion

There are three important fundamental issues that arise from analysis of the data presented in the previous section. The first is the consistency between an “end-to-end” simulation of the gyro-twt and the actual measured data. It turns out that simulations are not consistent with the measured data, so here we put forth plausible explanations for the inconsistencies. The second issue is to explain why the gyro-twt performed better with the wiggler guide field set well above the wiggler resonance value. The final issue is to address what effects space-charge may have had on the gyro-twt interaction.

We used the experimental run parameters for each of the gyro-twt run cases presented in Table 2 to simulate the performance of the gyro-twt from cathode to output window. Herrmannsfeldt’s EGUN[33] was used to model the initial electron beam. TRAJ was used to predict the beam propagation through the wiggler and to the start of the interaction region. The predicted beam spreads from TRAJ were then used as input to CRM32 to predict the gyro-twt efficiency. There are three significant unknowns in these experiments: the value of the pitch, parallel momentum spread, and energy spread of the electron beam upon entry into the gyro-twt interaction region. The values predicted for these quantities by TRAJ were typically $\alpha \sim 0.6$, $\sigma_{pz}/\langle p_z \rangle \sim 6\%$, and $\sigma_\gamma/\langle \gamma \rangle \sim 3\%$. When these values are used as input for CRM32, the result is almost negligible efficiency because the beam pitch is too low and/or the beam energy spread is too high. We believe that the CRM32 results, because they come from a well-benchmarked code based on well-developed theory, are more accurate than the TRAJ results. TRAJ has no self-axial fields, and therefore, in essence, is based on a paraxial beam assumption, which is not a good assumption for a beam corkscrewing through a wiggler with a pitch close to unity. For this reason, we believe the beam parameters upon

entry into the gyro-twt region were $\alpha \sim 0.9$, $\sigma_{pz}/\langle p_z \rangle \sim 12\%$, and $\sigma_\gamma/\langle \gamma \rangle \sim 3\%$. These values are consistent with power levels of 3–4 MW as predicted by CRM32, and they are also consistent with the predicted growth rate from CRM32, as shown in Fig. 7.

In almost all the cases in Table 2, the wiggler guide field was set well above the field value necessary for wiggler resonance. This parameter setting is where the experiments yielded the highest output power, even, in general, for the TE₂₁ case, though it is not shown in Table 2. When the gyro-twt is operated in this parameter space, the amplified pulses are limited in width compared to the linac voltage pulse (see Fig. 5) because the wiggler is resonant with the beam over a smaller range of voltages. This leads to narrow diamagnetic and rf pulses and increased phase variability over the rf pulse. Why, then did the gyro-twt experiments perform best in this situation? There are two plausible explanations. First, the beam quality may be substantially better when the wiggler guide field is set well above resonance. We have already questioned the validity of the TRAJ results, but the TRAJ simulations predict, in general, a 1–2% increase in energy spread (for the same end pitch value, α) when the wiggler is operated at resonance as opposed to off resonance. This increase is consistent with a sharp drop in gyro-twt efficiency as predicted by CRM32. The other plausible explanation is that running at conditions to try and widen the rf pulse typically resulted in increased power levels of competing instabilities and parasitic modes. This was observed experimentally. The lower frequency modes may have had deleterious effects on the amplification of the fundamental mode. The output window is also narrow band, so off-frequency modes are substantially reflected and able to re-amplify during wider pulses. The full explanation for running above wiggler resonance is likely a combination of the aforementioned factors.

The highest efficiency cases from the gyro-twt experiments all have relatively low measured beam currents of 100–150 A. These results are inconsistent with the CRM32 simulations, which predict relatively constant efficiency over a range of beam current up to at least 500 A for the experimental TE₃₁ gyro-twt operating parameters. This leads to speculation that at currents > 200 A, the space-charge forces of the beam begin to have a deleterious effect. The neglect of space charge is valid if the beam is tenuous, that is, if the plasma frequency of the beam is significantly less than the relativistic cyclotron frequency. R. Davidson, in Sec. 7.2 of his book[34], defines the following parameters related to space charge in a beam:

$$s_e \equiv \frac{\gamma \omega_p^2}{\Omega_{c0}^2} \quad (14)$$

$$s_e^0 \equiv \frac{2\beta_1^2}{(1 - \beta_z^2)^2} \quad (15)$$

Davidson's exact condition for a tenuous beam, then, is

$$s_e \ll s_e^0. \quad (16)$$

In the above equations, $\omega_p \equiv q_e \sqrt{n_e / (\epsilon_0 m_0)}$ is the plasma frequency, where n_e is the number of electrons per unit volume. The values of s_e/s_e^0 for the cases in Table 2 range from 0.07 (130 A case) to 0.19 (300 A case). The assumption is made here that the electron beam in the interaction region has a uniform 5 mm radius, as predicted by TRAJ, but a measurement done with a copper

strike plate shows a 3–4 mm radius, which would increase the estimated s_e/s_e^0 values by a factor of ~ 2 over those just mentioned. Equation 16 is the conclusion made for a free-space CRM dispersion relation with no wave-guide effects and no cyclotron harmonics included. Inclusion of these effects would be an important step to understanding how important space-charge effects are for the gyro-twt operating parameters. The lower efficiencies at higher beam currents are certainly suggestive of a deleterious effect from increased space charge.

7 Summary

We have presented here results from the first multi-megawatt (4 MW, $\eta = 8\%$) harmonic relativistic gyrotron traveling-wave tube amplifier experiment. The first ever third harmonic gyro-twt results are reported, and the first detailed phase measurements of gyro-twt operation are also shown. The purpose of these experiments was to demonstrate high power, high gain amplification at 17.1 GHz. Beam parameters of $\alpha \sim 0.9$, $\sigma_{pz}/\langle p_z \rangle \sim 12\%$, and $\sigma_\gamma/\langle \gamma \rangle \sim 3\%$ are consistent with the measured power according to the results from large signal steady-state numerical simulations.

High power amplification was observed for both the third harmonic and the second harmonic experiments. The third harmonic experiment generated 4 MW of amplified rf power in the TE₃₁ mode with 50 dB measured gain and ± 2 dB absolute error attributable to measurement inaccuracies. The highest measured efficiency was 8% at 3.5 MW of rf power. The second harmonic experiment yielded 2 MW rf power and 4% efficiency with a measured gain of 40 dB. The measured rf pulses are narrow in comparison to the voltage pulse, with the typical width being 10–15 ns. In addition, a characteristic frequency upchirp of ~ 10 MHz/ns was measured on the rf pulses and is attributable to the rounded top of the voltage pulse and, correspondingly, the beam pitch profile. The best measured phase stability of the high power TE₃₁ amplified pulses was $\pm 10^\circ$ over a 9 ns duration and $\pm 20^\circ$ over a 15 ns duration. These measurements were made on 3 MW pulses.

The experimental results presented here demonstrate the unique combination of stability and high power at high frequencies promised by the harmonic gyro-twt, even when beam quality is not ideal. The most promising area for the harmonic gyro-twt is likely at the 95 GHz frequency, where a high-gain, high-power amplifier is aggressively being pursued by both industry and the government due to the 95 GHz propagation window in the earth's atmosphere. A third (or higher) harmonic gyro-twt could conceivably generate a 95 GHz amplified pulse without the use of a superconducting magnet. The results presented here suggest that to be a successful contender, such a harmonic gyro-twt should not use a Pierce-wiggler beam formation system due to the poor resulting beam quality, particularly the high energy spread. Also, a multi-sectioned interaction with severs would reduce competing instabilities for long pulses.

8 REFERENCES

References

- [1] W. Lawson, H.W. Matthews, M.K.E. Lee, J.P. Calame, B. Hogan, J. Cheng, P.E. Latham, V.L. Granatstein, and M. Reiser. High-power operation of a k-band second-harmonic gyrokystron. *Phys. Rev. Lett.*, 71(3):456–459, July 1993.
- [2] Q.S. Wang, D.B. McDermott, and Jr. N.C. Luhmann. Characteristics of a stable 200 kw second-harmonic gyro-twt amplifier. In *Tech. Dig., IEEE Int. Electron Devices Meeting*, pages 231–234. IEEE, 1995.
- [3] K.R. Chu, L.R. Barnett, H.Y. Chen, S.H. Chen, C. Wang, Y.S. Yeh, Y.C. Tsai, T.T. Yang, and T.Y. Dawn. Stabilization of absolute instabilities in the gyrotron traveling wave amplifier. *Phys. Rev. Lett.*, 74:1103–1106, 1995.
- [4] S.H. Gold, D.A. Kirkpatrick, A.W. Fliflet, R.B. McCowan, A.K. Kinkead, D.L. Hardesty, and M. Sucey. High-voltage millimeter-wave gyro-traveling-wave-amplifier. *J. Appl. Phys.*, 69, 1991.
- [5] R.S. Symons, H.R. Jory, S.J. Hegji, and P.E. Ferguson. An experimental gyro-twt. *IEEE Trans. Microwave Theory Tech.*, 29(3):181–184, 1981.
- [6] K.C. Leou, D.B. McDermott, F.V. Hartemann, S.N. Fochs, and Jr. N.C. Luhmann. Initial operation of a wideband gyro-twt amplifier. In *Tech. Dig., IEEE Int. Electron Devices Meeting*, pages 359–362. IEEE, 1993.
- [7] W.L. Menninger. *Relativistic Harmonic Gyrotron Traveling-Wave Tube Amplifier Experiments*. PhD thesis, MIT, 1994.
- [8] A.T. Lin, K.R. Chu, C.C. Lin, C.S. Kou, D.B. McDermott, and Jr. N.C. Luhmann. Marginal stability design criterion for gyro-TWTs and comparison of fundamental with second harmonic operation. *Int. J. Electron.*, 72(5–6):873–885, 1992.
- [9] P. Sprangle and T. Coffey. New sources of high-power coherent radiation. *Physics Today*, 37(3):44–51, 1984.
- [10] J. Schneider. Stimulated emission of radiation by relativistic electrons in a magnetic field. *Phys. Rev. Lett.*, 2(12):504–505, 1959.
- [11] A.V. Gaponov, M.I. Petelin, and V.K. Yulpatov. The induced radiation of excited classical oscillators and its use in high-frequency electronics. *Radiophys. Quantum Elect.*, 10(9–10):794–813, 1967.
- [12] M.I. Petelin. On the theory of ultrarelativistic cyclotron self-resonance masers. *Radiophys. Quantum Elect.*, 17:686–690, 1974.

- [13] P. Sprangle and A.T. Drobot. The linear and self-consistent nonlinear theory of the electron cyclotron maser instability. *IEEE Trans. Microwave Theory Tech.*, 25:528–544, 1977.
- [14] N.S. Ginzburg, I.G. Zarnitsyna, and G.S. Nusinovich. Theory of cyclotron-resonance maser amplifiers. *Radiophys. Quantum Elect.*, 24:331–338, 1981.
- [15] V.L. Bratman, G.G. Denisov, N.S. Ginzburg, and M. I. Petelin. FELs with bragg reflection resonators: Cyclotron autoresonance masers versus ubitrons. *IEEE J. Quantum Electron.*, QE-19:282–296, 1983.
- [16] K. E. Kreischer and R. J. Temkin. High frequency gyrotrons and their application to tokamak plasma heating. In *Infrared and Millimeter Waves*, volume 7, chapter 8. Academic Press, 1983.
- [17] A.W. Fliflet. Linear and nonlinear theory of the Doppler shifted cyclotron resonance maser based on TE and TM waveguide modes. *Int. J. Electron.*, 61:1049, 1986.
- [18] C. Chen and J.S. Wurtele. Efficiency enhancement in cyclotron autoresonance maser amplifiers by magnetic field tapering. *Phys. Rev. A*, 40:489, 1989.
- [19] G.S. Nusinovich. Cyclotron resonance masers with inhomogeneous external magnetic fields. *Phys. Fluids B*, 4(7):1989–1997, 1992.
- [20] K.D. Pendergast, B.G. Danly, R.J. Temkin, and J.S. Wurtele. Self-consistent simulation of cyclotron autoresonance maser amplifiers. *IEEE Trans. Plasma Sci.*, PS-16(2):122–128, 1988.
- [21] H. Freund and C. Chen. Comparison of gyro-averaged and non-gyro-averaged nonlinear analyses of cyclotron autoresonance masers. *Int. J. Electron.*, 72:1005–1031, 1992.
- [22] Q.S. Wang, C.S. Kou, D.B. McDermott, A.T. Lin, K.R. Chu, and Jr. N.C. Luhmann. High-power harmonic gyro-TWT's—part ii: nonlinear theory and design. *IEEE Trans. Plasma Sci.*, 20(3):163–169, 1992.
- [23] K.R. Chu and J.L. Hirshfield. Comparative study of the axial and azimuthal bunching mechanisms in electromagnetic cyclotron instabilities. *Phys. Fluids*, 21:461, 1978.
- [24] C. Chen, B.G. Danly, J.A. Davies, W.L. Menninger, J.S. Wurtele, and G. Zhang. CARM amplifier theory and simulation. *Nucl. Instr. Methods Phys. Res. A*, A304:593–600, 1991.
- [25] D.L. Goodman, D.L. Birx, and B.G. Danly. Induction linac driven relativistic klystron and cyclotron autoresonance maser experiments. In H.E. Brandt, editor, *Intense Microwave and Particle Beams II*, pages 217–225. SPIE, 1991.
- [26] K.D. Pendergast. *Theoretical and Experimental Research on a High-Power, High-Frequency Cyclotron Autoresonance Maser*. PhD thesis, MIT, 1991.
- [27] G. Vasilakos. Simulation of an electron beam in a helical wiggler, 1990. Bachelor's Thesis, Massachusetts Institute of Technology.

- [28] J.A. Smolin. Simulation and measurement of an electron beam in a wiggler magnetic field, 1989. Bachelor's Thesis, Massachusetts Institute of Technology.
- [29] A. Li. Analysis of the radiation pattern from a quasi-optical antenna. Master's thesis, MIT, 1991.
- [30] W.H. Press, B.P. Flannery, S.A. Teukolsky, and W.T. Vetterling. *Numerical Recipes in C*. Cambridge University Press, Cambridge, England, 1988.
- [31] R.E. Collin. *Antennas and Radiowave Propagation*. McGraw-Hill, New York, 1985.
- [32] J. Gonichon. *PhD. Thesis*. PhD thesis, Université Paris VII, 1994.
- [33] W.B. Herrmannsfeldt. Electron trajectory program. Technical Report SLAC-226, UC-28, Stanford Linear Accelerator Center, 1979.
- [34] R.C. Davidson. *Physics of Nonneutral Plasmas*. Addison-Wesley, Reading, MA, 1990.